CrystEngComm

Cite this: *CrystEngComm*, 2012, **14**, 5589–5595

www.rsc.org/crystengcomm

PAPER

Architecture controlled synthesis of flower-like In_2O_3 nanobundles with significantly enhanced ultraviolet scattering and ethanol sensing†

Hsiang-Yu Lai,[a] Tsung-Han Chen[a] and Chun-Hua Chen*[b]

Received 3rd March 2012, Accepted 25th May 2012
DOI: 10.1039/c2ce25310k

We have successfully synthesized novel needle-like and flower-like In_2O_3 nanobundles (NBs) composed of numerous parallel assembled nanoparticle chains *via* hydrolysis of $InCl_3$ with $NaBH_4$ in aqueous solution and subsequent heat treatment. These previously unknown nanostructures exhibit unusual optical and ethanol sensing properties. T-matrix simulation evidently explains the assembling effect on the significant scattering of UV-visible spectra including a characteristic peak in the UV region as well as the broadened edge toward the visible region for these two NBs. The greatly enhanced ethanol-sensing properties observed for the flower-like In_2O_3 NBs indicate that the dominant factors for sensing are not only the nanoparticle size but also the structural dimension and architecture of the nanoassembly.

Introduction

Oxide nanostructures of various dimensions, morphologies and sizes have been widely designed, produced, investigated and subsequently applied in a variety of fields in the past decades.[1–4] Among these researches, controlled synthesis of novel architectures assembled from low-dimensional building blocks has become the most important and interesting topic from both academic and industrial viewpoints since it is the gateway to exploring distinct physical and chemical fundamentals and corresponding advanced applications such as photocatalysts,[5] gas sensors,[6] biosensors,[7] and energy storage.[8]

Indium oxide (In_2O_3) known as a promising gas sensing material has shown superior performance for detecting the presence of reducing gases such as CO and C_2H_5OH as well as oxidizing gases such as NO_2 and O_3.[9–11] Many research efforts have focused on designing novel well-defined In_2O_3 secondary architectures organized by primary nano-units for sensor applications. Such In_2O_3 architectures exhibit open channels for gas diffusion, high surface to volume ratio for gas species absorption/desorption, and low-resistance pathways for charge carrier transport, and thus exhibit faster response times, higher sensitivity, better selectivity and lower limits of detection.[12–15] Moreover, In_2O_3 assembled nanostructures have also been found to exhibit unique optical properties in UV-visible adsorption and photoluminescence, unlike isolated nanostuctures.[16–19] Given these achievements, it is worthwhile to deeply explore In_2O_3 assembled architectures not only for finely understanding structure and morphology-dependent optical properties, to improve functional applications such as in sensors, but also to investigate the self-assembly strategy for such nanostructures.

Recently, various novel In_2O_3 self-assembled nanostructures have been fabricated mainly using chemical approaches, for instance, hollow spherical nanostructures made of well-aligned nanocubes,[20] nanorod bundles and spheres composed of nanorods,[21] hollow spheres consisting of nanoflakes,[22] and micro-pompons composed of nanobipyramids.[23] Although these In_2O_3 nanostructures with geometric features can be easily and effectively fabricated by annealing well-designed, special and suitable $In(OH)_3$ or In_2S_3 precursors, the hydrothermal processing frequently applied for the synthesis of these precursors is a drawback due to the relatively high pressure and temperatures needed and the very time-consuming nature.

In this work, a facile surfactant-free solution approach has been developed to synthesize $In(OH)_3$ precursors exhibiting novel needle-like and flower-like nanobundle (NB) structures. The solution route is simple, convenient, time-saving and high-throughput, features which are in contrast to typical hydrothermal processes. However, under such solution-based reaction conditions, namely the relatively low ambient pressure and temperature, large changes in the product morphologies cannot always be expected. Until now, only very limited pioneering progress in the synthesis of assembled In_2O_3 nanostructures *via* solution routes has been demonstrated.[14,24] Control of the assembled nanostructures to design architectures of various dimensions *via* the solution approach is a considerable challenge.

By precisely controlling the temperature of the aqueous solution, the morphology of $In(OH)_3$ NB changed from needle-like to a flower-like shape without the assistance of

[a]*Department of Materials Science and Engineering, National Chiao Tung University, 1001 Ta-Hsueh Road, Hsin-Chu, 30010, Taiwan, ROC. E-mail: hsiang.mse96g@g2.nctu.edu.tw*
[b]*Department of Materials Science and Engineering, National Chiao Tung University, 1001 Ta-Hsueh Road, Hsin-Chu, 30010, Taiwan, ROC. E-mail: ChunHuaChen@mail.nctu.edu.tw*
† Electronic supplementary information (ESI) available. See DOI: 10.1039/c2ce25310k

templates or surfactants. After the subsequent dehydration process at high temperatures, In_2O_3 NBs were obtained with retention of morphology. In order to qualitatively and quantitatively distinguish the effect of aggregation with different morphologies on the UV-visible spectra, careful theoretical simulation was carried out to allow comparisons to be made. In the ethanol-sensing characterizations, these quasi-ordered secondary assemblies obviously show great potential for gas detection; however, relative data are still lacking owing to the technological difficulty of fabrication. Here, both needle-like and flower-like In_2O_3 NBs were applied as ethanol sensors in order to explore the morphology-dependent sensing properties.

Experimental section

All chemicals used in this work were analytical grade and were used without further purification. To synthesize the $In(OH)_3$ structural precursors required for obtaining In_2O_3 needle-like and flower-like NBs, $InCl_3{\cdot}4H_2O$ (0.1 mmol) was dissolved into 25 ml of distilled water. On adding 25 ml of $NaBH_4$ solution (0.05 mM) to the prepared $InCl_3$ solutions kept at 40 or 50 °C under stable stirring, white precipitates immediately formed which were identified as needle-like and flower-like NBs of $In(OH)_3$, respectively. The $In(OH)_3$ precursors were collected by centrifugation at 10 000 rpm for 5 min and were then repeatedly washed with distilled water to remove residual chemicals. After drying at 60 °C in air, the $In(OH)_3$ precursors were heated at 500 °C in air for 2 h to obtain In_2O_3 nanostructures.

The crystal structures of the prepared nanostructures were identified by X-ray diffraction (XRD, D2 Phaser, Bruker AXS) with Cu-Kα radiation (λ = 1.5418 Å). The morphologies were determined by field-emission scanning electron microscopy (FESEM, JEOL JSM-6700F). For high-resolution transmission electron microscope (HRTEM, JEOL-2010) and selected area electron diffraction (SAED) analyses, a few drops of the dispersions were placed onto carbon-coated copper grids and dried at room temperature in a vacuum. The UV-visible spectra were recorded with a UV-visible spectrophotometer (Evolution 300). The Brunauer–Emmett–Teller (BET) surface areas of prepared In_2O_3 nanostructures were determined by nitrogen adsorption–desorption isotherms at 77 K (NOVA 1000e).

To fabricate the gas sensors, first, gold electrodes were fabricated on an alumina substrate and a ruthenium oxide (RuO_2) heater was coated on the back of the substrate. The washed $In(OH)_3$ nanostructures were re-suspended in distilled water to form a colloidal solution and then coated onto the prepared substrate. The dried $In(OH)_3$ sensors were calcined at 500 °C for 2 h in air to convert $In(OH)_3$ into In_2O_3 for gas sensing. The prepared In_2O_3 sensor was placed in a sealed chamber and aged at 400 °C for 5 h to stabilize it. After this, the target ethanol gas of a specific concentration was injected into the chamber, and the change in resistance was measured immediately. The gas sensitivity is defined as $S = R_a/R_g$, where R_a and R_g are the electrical resistances of the sensor in air and in ethanol gas, respectively.

Results and discussion

Fig. 1 shows the XRD patterns of the white precipitates prepared by reaction of $InCl_3$ with $NaBH_4$ at 40 and 50 °C, respectively.

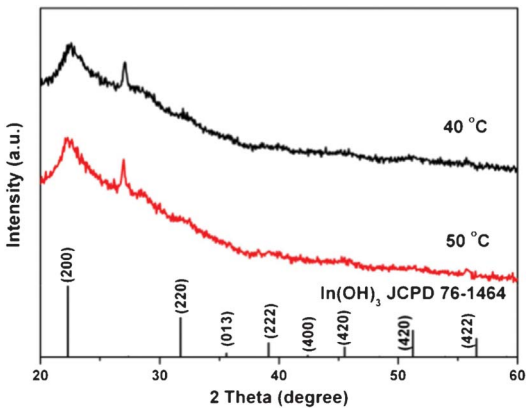

Fig. 1 XRD patterns of $In(OH)_3$ synthesized by the solution route at 40 and 50 °C.

Obviously, all the extremely wide peaks of both patterns can be indexed well as body-centered cubic $In(OH)_3$ (JCPDS 76-1464) except for the somewhat sharper peaks around 27°–29°, which probably result from chloride and boron derivatives, for example boron chloride (JCPDS No. 73-2137) and boric acid (JCPDS No. 78-0470). Even though In^{3+} should be reducible to In^0 by BH_4^- based on standard reduction potentials ($E^\circ_{In^{3+}/In^0}$ = −0.338 eV, $E^\circ_{B(OH)_3/BH_4^-}$ = −0.481 eV),[25] metallic indium is not observed, mainly due to the relatively low standard reduction potential compared with noble metals[26–29] (*e.g.* $E^\circ_{Au^{3+}/Au^0}$ = +1.5 eV and $E^\circ_{Ag^+/Ag^0}$ = +0.8 eV) and more importantly because of hydrolysis of $NaBH_4$ in aqueous solutions.

Thus non-aqueous solvents have been used by researchers for successfully obtaining isolated metallic indium nanoparticles with $NaBH_4$.[25,30–32] According to their results, naked metallic indium nanoparticles do not seem to provide a meaningful self-assembly mechanism to achieve a variety of architectures and thus were not our target products. In the present aqueous reaction with $NaBH_4$, the formation of $In(OH)_3$ by hydrolyzing In^{3+} at these two close temperatures, 40 and 50 °C, is as expected since previous research has evidenced the hydrolysis reaction of $NaBH_4$ in water.[33]

The FESEM images shown in Fig. 2a and b, as expected, clearly reveal two types of assemblies with a high uniformity and similar scale, which are referred to as needle-like and flower-like $In(OH)_3$ NBs, respectively. Obviously, these two structures seem to have the same unit blocks, that is, needle-like NBs. It is thus reasonable to consider that with the increase in reaction temperature from 40 to 50 °C, another assembly mechanism was activated to cause the formation of flower-like NBs compared with the randomly stacked needle-like ones. As can be seen in Fig. 2c, the branched tips observed in the TEM image of isolated needle-like $In(OH)_3$ NBs directly evidence that the significant bundled structures are assemblies of numerous nanorods arranged side by side. Fig. 2d shows the SAED pattern recorded from the central region of an $In(OH)_3$ NB. The diffuse spots arranged in a hexagonal symmetry indicate that the $In(OH)_3$ NB, which contains numerous nanorods, exhibits a significant cubic [110] orientation along its 1D morphology.

According to these observations, a possible mechanism is proposed to explain the self-assembling of $In(OH)_3$ nanorods. At the initial stage, tiny $In(OH)_3$ nanorods promptly form through

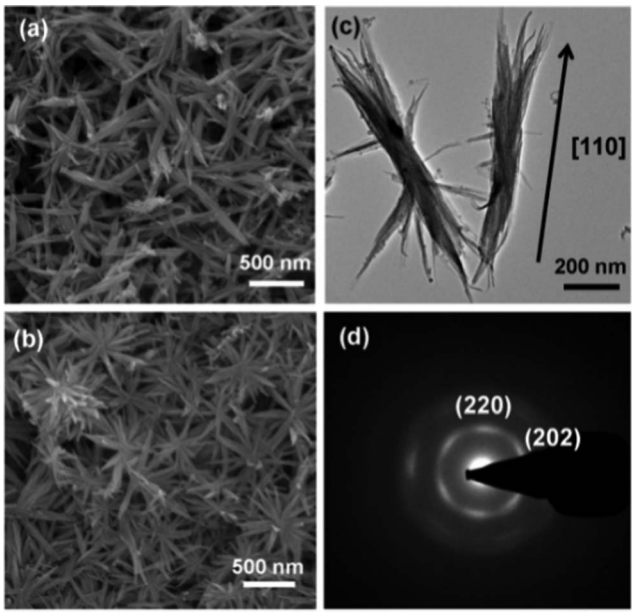

Fig. 2 FESEM images of (a) $In(OH)_3$ needle-like NBs and (b) $In(OH)_3$ flower-like NBs. (c) TEM image of the branched tips observed in isolated needle-like $In(OH)_3$ NBs. (d) SAED pattern recorded from the central region of an $In(OH)_3$ NB.

a hydrolysis reaction. When the tiny $In(OH)_3$ nanorods come close to each other, a condensation reaction could happen between the hydroxyl groups (–OH) present on the surfaces of the nanorods to build chemical bonds, oxo (–O–) bridges.[34,35] The tiny $In(OH)_3$ nanorods thus assemble in an ordered manner by end-to-end as well as side-to-side arrangements along the [110] direction to form longer and more coarsely oriented assembled NBs. However, if only the formation mechanism of oriented-attachment were operative, pillar-ended NBs should be the main product as found by Wei.[36] On close observation of the tip parts of the $In(OH)_3$ NBs as shown in Fig. 2c, we believe that numerous sharp and smooth branched nanorods should be the result of anisotropic crystal growth. During the rapid construction of $In(OH)_3$ NBs by oriented assembling $In(OH)_3$ nanorods, the free surface of the bound nanorods must keep growing to have such sharp tips.

Regarding the formation mechanism of the flower-like $In(OH)_3$ NBs, it is reasonable to consider that such a three-dimensional radiating architecture should originate from a branched nucleus which might be composed of numerous randomly assembled tiny $In(OH)_3$ nanorods. Since the $In(OH)_3$ nanorods are extremely tiny at the very initial stage, a synthesis temperature of 50 °C seems high enough to fuse and stabilize any randomly attached tiny $In(OH)_3$ nanorods to form branched $In(OH)_3$ nuclei. With the continuous growth of the tiny $In(OH)_3$ nanorods, the temperature can no longer drive the formation of branched nuclei. The growth mechanism will then be governed by the oriented assembling mechanism dominated by –OH groups as described above, to lead to distinct flower-like NBs.

The $In(OH)_3$ needle-like and flower-like NBs were then dehydrated at 500 °C and the XRD patterns shown in Fig. 3 clearly evidence that complete phase transformation from $In(OH)_3$ to In_2O_3 (JCPD 76-0152) was achieved. The morphological

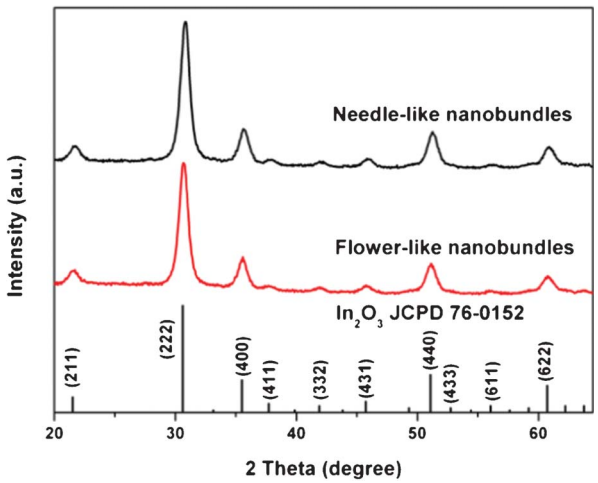

Fig. 3 XRD patterns of In_2O_3 needle-like and flower-like NBs synthesized by calcination.

investigations of these two NBs are shown in Fig. 4 and 5, respectively. As can be seen in the corresponding FESEM images (Fig. 4a and 5a), the obtained In_2O_3 nanostructures after annealing basically maintain their former $In(OH)_3$ morphologies, that is, the needle-like and flower-like morphologies[37,38] but the average outline size decreases slightly due to the dehydration. However, the small difference between the XRD patterns (Fig. 3) indicates the absence of morphology-induced preferential orientation. The TEM images of an isolated In_2O_3 needle-like NB and its tip zone shown in Fig. 4b and 4c, respectively, clearly display numerous parallel and uniformly sized tightly bundled nanochains. From the contrast found within each nanochain (Fig. 4c) and the coherent

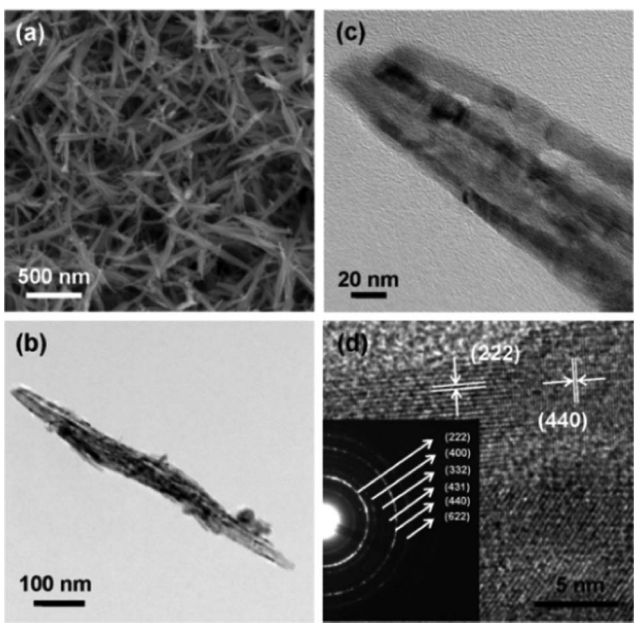

Fig. 4 (a) FESEM image of In_2O_3 needle-like NBs. (b) TEM image of an individual In_2O_3 needle-like NB. (c) TEM image of tip part of needle-like NBs composed of numerous nanoparticles. (d) HRTEM image of needle-like NBs showing that two grains have clear (222) planes and (440) planes; (inset) SAED patterns showing the polycrystalline structure.

length of lattice fringes (Fig. 4d), each nanochain should be constructed from numerous nanoparticles with diameters of ~10 nm compactly connected along one dimension instead of a single crystal. The observed TEM nanoparticle size is coincident with the crystalline size estimated by the Scherrer equation from the full-width at half-maximum (FWHM) of the (222) peak (Fig. 3). In contrast to the diffuse spots observed in Fig. 2d, the broken rings of the corresponding SAED pattern (Fig. 4d, inset) recorded from the central part of an In_2O_3 bundle show that the preferential orientation still exists after dehydration, but the misorientation largely increases, probably due to the volume shrinkage from $In(OH)_3$ nanorods to In_2O_3 nanochains. The morphology of the In_2O_3 flower-like NBs observed in the SEM image (Fig. 5a) basically follows that of the $In(OH)_3$ ones and is quite uniform.

The TEM image of an individual In_2O_3 flower-like NB shown in Fig. 5b obviously shows that all branches are solidly conjoined at one centre point. Like the above needle-like NBs, each branch of the flower-like NBs is constructed from numerous nanochains (see Fig. 5c). This distinct morphology suggests that the flower-like NB is an evolutional form from the needle-like NBs. As shown in Fig. 5d, the different nanoparticles within each NB have an interplanar spacing of 0.292 nm, which corresponds to the (222) planes of cubic In_2O_3. The broken SAED rings diffracted from the flower-like NBs originated for the same reason as indicated in Fig. 4d.

Fig. 6a shows the normalized UV-visible extinction spectra of the In_2O_3 needle-like and flower-like NBs suspended in water. A couple of interesting features, that is, a characteristic peak around 307 nm and a wide edge toward the visible region, can be clearly observed for both NBs. Generally, a very sharp absorption edge should be found in the UV region for well-suspended In_2O_3 nanoparticles in solution because In_2O_3 is a

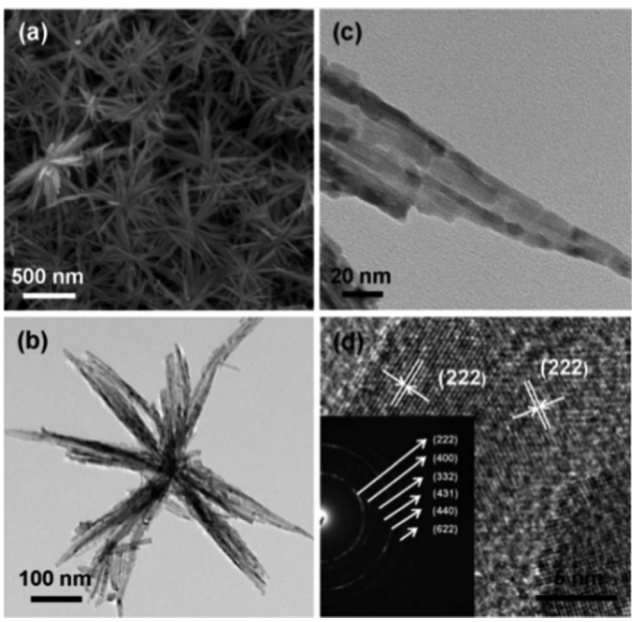

Fig. 5 (a) FESEM image of In_2O_3 flower-like NBs. (b) TEM image of In_2O_3 single flower-like NB. (c) TEM image of tip part of a branch of flower-like NBs composed of numerous nanoparticles. (d) HRTEM image of flower-like NBs shows clear (222) planes from two grains; (inset) SAED patterns showing the polycrystalline structure.

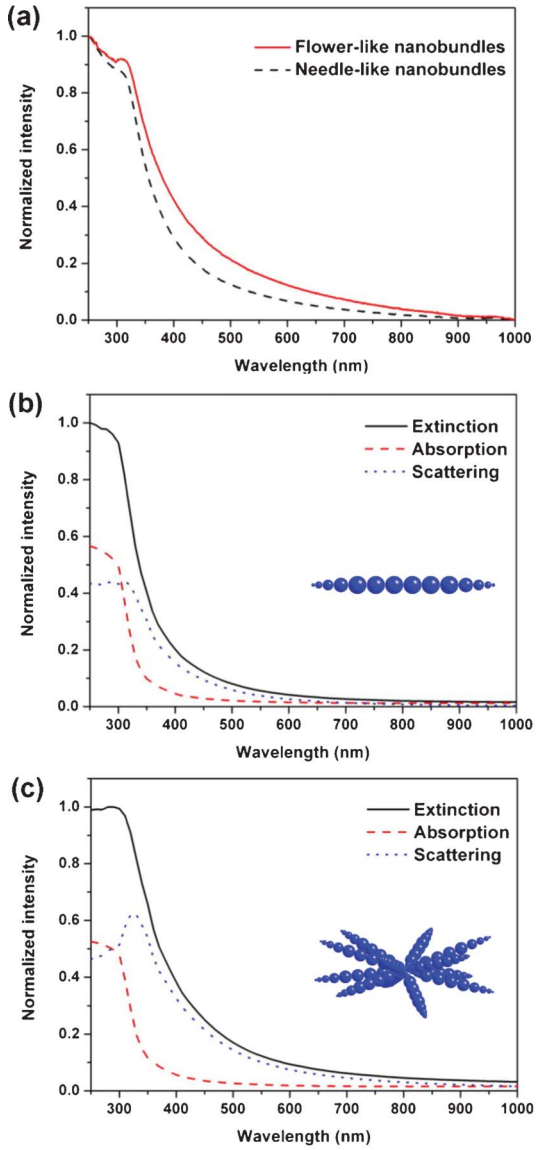

Fig. 6 (a) UV-visible extinction spectra of In_2O_3 NBs and calculated spectra of extinction (solid line), absorption (dashed line), and scattering (dotted line) for (b) needle-like shape and (c) flower-like shape. (Inset, b) Model of needle-like shape. (Inset, c) Model of flower-like shape.

wide bandgap semiconductor.[39] We have previously qualitatively demonstrated the aggregation effect of In_2O_3 nanoparticles on UV-visible spectra by comparing the spectra of assembled and isolated In_2O_3 nanoparticles.[40] Thus it is easy to understand that these two characteristics shown in Fig. 6a originate not only from the NBs but also from the assembly of NBs. However, without further theoretical analysis, it is impossible to quantitatively clarify the differences in the spectra between these two NBs.

In this work, we introduce a numerical method called the T-matrix to respectively calculate theoretical UV-visible extinction, absorption and scattering spectra of these two assemblies to gain a fundamental understanding of the observed difference in spectra. This numerical analysis has been widely applied to compute light scattering for single non-spherical particles with large size parameters and/or extreme geometries and composite/

aggregated particles.[41] The T-matrix approach, based on solving Maxwell's equations, used the superposition formulation for radiative interactions among aggregated spheres, in which the total scattered field from the ensemble of spheres is described as a superposition of vector spherical harmonic expansion (VSWF) of the scattered field from each individual sphere in the aggregated spheres.[42,43] The general formulation and procedure of the mathematical simulation of the T-matrix for assembled nanoparticles have been described in detail elsewhere.[44]

In order to reasonably simplify the complicated calculation, we assume that the needle-like assembly is constructed of several hard spheres arranged along one direction with suitable diameters as displayed in the inset of Fig. 6b. With the same idea, the hard-sphere model of the flower-like assembly is accordingly designed as shown in the inset of Fig. 6c. The structural parameters including the size, diameter and morphology of these two models are entirely based on observation of SEM and TEM images. Fig. 6b and c show the calculated extinction spectra and their components, the absorption and scattering ones. It is found that the extinction spectra fit the experimental ones excellently (see Fig. 6a), including the peak top and the broad edge. The present result indicates that the equivalent hard-sphere assumption can be accepted and considered as a suitable simplified approach for modeling complicated nanoparticle-assembly-like NBs. The extinction spectrum is a summation of the absorption and scattering spectrum. It is easy to understand that the calculated absorption spectra for both assemblies are rather similar, as can be seen in Fig. 6b and c, mainly due to the similar intrinsic properties of the In_2O_3 spheres with similar size distributions. Therefore, the specific differences of a characteristic peak and a wide edge toward the visible region that appeared between the extinction profiles of these two assemblies are certainly dominated by the scattering spectra. In addition, the somewhat higher scattering band found for flower-like NBs would have originated from the assembly of NBs. Based on the above theoretical decomposition, here we want to emphasize that the extinction spectra, and more precisely the scattering spectra, can truly reflect the assembly characteristics. Recently, by controlling the size and morphology of oxide nanostructures applied as scattering layers of dye-sensitized solar cells, it was found that the light scattering can be tuned and enhanced to effectively improve solar-to-electric conversion efficiency.[45,46] Our present spectra and the corresponding T-matrix simulation could provide a fundamental understanding of the nanostructure-dependent scattering of oxides for further design of advanced dye-sensitized solar cells.

The dynamic ethanol gas sensing of the needle-like and flower-like NBs under various ethanol concentrations was carried out and the measured response–recovery curves are shown in Fig. 7a and b, respectively. For the purpose of comparison, zero-dimensional In_2O_3 nanoparticles $\sim$10 nm in diameter synthesized by the same processes but replacing $NaBH_4$ with NH_4OH were also fabricated (Fig. S1, ESI†) and the sensing result is shown in Fig. 7c. As displayed, when ethanol gas is injected into the chamber, the response resistance immediately decreases. As the ethanol gas is withdrawn from the chamber and replaced with dry air, the resistance recovers to the initial state. The reasonable mechanism of ethanol sensing of In_2O_3 reported elsewhere is briefly summarized as below.[47] At first, O_2

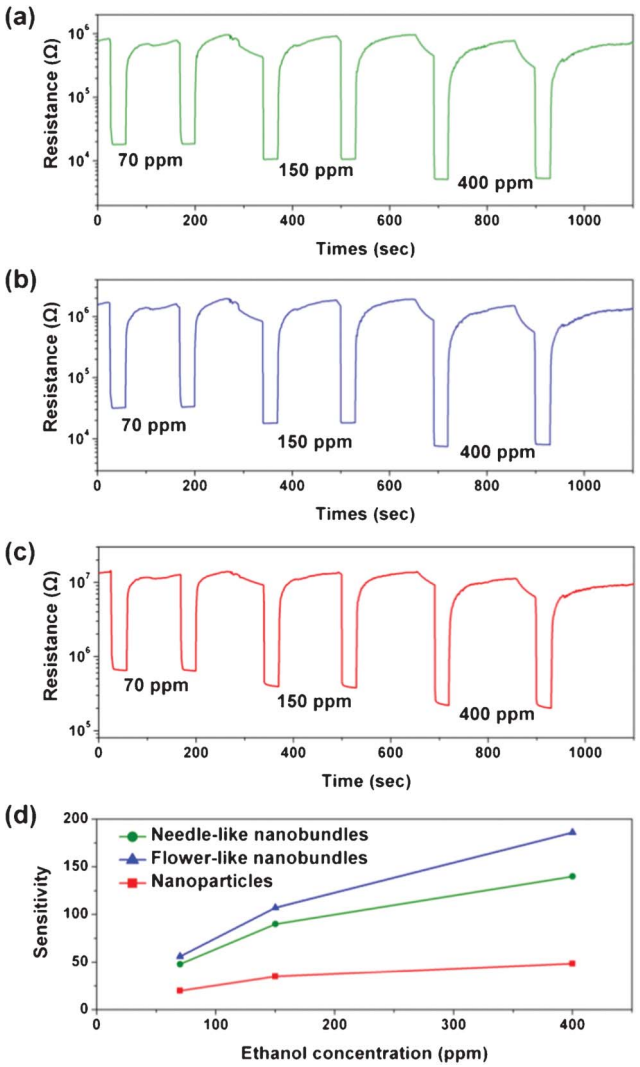

Fig. 7 Dynamic ethanol-sensing properties of In_2O_3 nanostructures at a series of ethanol concentrations ranging from 70 to 400 ppm: (a) needle-like NBs, (b) flower-like NBs, (c) nanoparticles and (d) gas sensitivity (R_a/R_g) *vs.* ethanol concentration.

molecules absorbed on the In_2O_3 surface capture electrons from the conduction band to produce negative oxygen species such as O_2^-, O^- and O^{2-}, which lead to the formation of an electron depleted region on the In_2O_3 nanoparticle surface. When In_2O_3 is exposed to ethanol gas, ethanol molecules react with oxygen ions absorbed on In_2O_3. The electrons trapped by oxygen species are re-injected into In_2O_3 and decrease the thickness of the electron depleted region, thereby leading to a decrease in resistance. Fig. 7d shows the ethanol concentration dependent sensitivity for each type of In_2O_3 sensor.

Obviously, the ethanol sensing sensitivity greatly depends on the assembled conditions of In_2O_3. The In_2O_3 NBs exhibit significantly higher sensitivity than the nanoparticle films. For detection of 70 ppm ethanol, the needle-like NBs and flower-like bundles show high gas sensitivity values of 45 and 50, which is over three times larger than that of zero-dimensional nanoparticles. This is probably due to the relatively high packing density of spherical nanoparticles in the films. Earlier researches suggested that nanoparticle size is the primary factor that

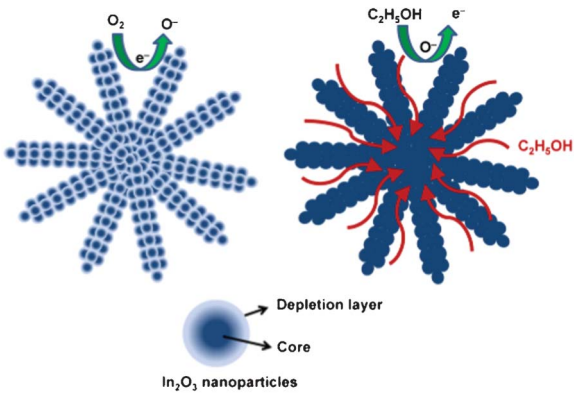

Fig. 8 Scheme of ethanol sensing mechanism for flower-like In_2O_3 NBs.

effectively improves gas sensing performance.[48,49] When the particle size is close to or less than twice the thickness of the depleted region, the depleted region is full of whole grains or particles, which is the optimum situation for response and sensitivity.[50,51] However, the solution-based zero-dimensional nanoparticles generally tend to develop dense agglomeration and higher packing density after spreading on substrates as a solid-state sensor, which dramatically decreases most activated surface areas and thus limits performance enhancement by decreasing the crystal size.[50] The BET specific surface area of the needle-like NBs and the flower-like NBs, 51.6 and 54.2 $m^2\ g^{-1}$, respectively, are significantly larger than the 19.6 $m^2\ g^{-1}$ of zero-dimensional nanoparticles (Fig. S2, ESI†). The BET result is consistent with the sensing performance of each sensor type and directly evidences our viewpoint. The random stacking of one- or three-dimensional nanoparticle-assembled NBs as presented here could lead to high surface to volume ratios for gas absorption/desorption and also provide numerous open channels that would enable target gases to easily diffuse into the inner part of the stacks and thus enhance the response of the target gases.[12,15] The above described mechanisms are illustrated in Fig. 8.

From structural investigation and sensing characterization, we have clearly proven that the gas sensing properties are predominantly affected by stacking configuration, which can be indirectly controlled by the synthesis of nano-assemblies with suitable architectures. It is worth emphasizing here that the present nanoparticle-assembly-like NBs, which couple the advantages of the zero- and higher-dimensional nanostructures, ideally fit the structural requirements for sensor related applications.

Conclusions

Novel In_2O_3 needle-like and flower-like NBs assembled from numerous 1D nanochains have been successfully synthesized *via* dehydration of $In(OH)_3$. The assembling effect of nanoparticles within the In_2O_3 NBs results in a striking appearance of a characteristic peak at around 307 nm, and obvious broad bands in the visible region of the UV-visible spectrum have been reproduced by T-matrix simulation. These calculations allow us to identify not only the important features in the spectra of the NBs but also the relation between morphologies and spectra. In ethanol sensing measurements, the In_2O_3 NBs exhibit morphology-dependent gas sensing properties and an improved gas sensitivity due to higher-dimensional architectures. The discovery of these previously unknown In_2O_3 NBs and their unusual optical and sensing properties points to a way of developing advanced gas sensors on the basis of assembly morphology in addition to nanoparticle size.

References

1 H. Zeng and S. Sun, *Adv. Funct. Mater.*, 2008, **18**, 391.
2 D. P. Liu, G. D. Li, Y. Su and J. S. Chen, *Angew. Chem., Int. Ed.*, 2006, **45**, 7370.
3 W. S. Seo, H. H. Jo, K. Lee and J. T. Park, *Adv. Mater.*, 2003, **15**, 795.
4 N. Wang, X. Cao, Q. Wu, R. Zhang, L. Wang, P. Yin and L. Guo, *J. Phys. Chem. C*, 2009, **113**, 21471.
5 L. Liu, H. Liu, Y. P. Zhao, Y. Wang, Y. Duan, G. Gao, M. Ge and W. Chen, *Environ. Sci. Technol.*, 2008, **42**, 2342.
6 Y. Zhang, J. Xu, Q. Xiang, H. Li, Q. Pan and P. Xu, *J. Phys. Chem. C*, 2009, **113**, 3430.
7 C. Xia, N. Wang, L. Lidong and G. Lin, *Sens. Actuators, B*, 2008, **129**, 268.
8 F. Cheng, J. Zhao, W. Song, C. Li, H. Ma, J. Chen and P. Shen, *Inorg. Chem.*, 2006, **45**, 2038.
9 G. Neri, A. Bonavita, G. Micali, E. Rizzo and G. Callone, *Sens. Actuators, B*, 2008, **132**, 224.
10 C. Xiangfeng, W. Caihong, J. Dongli and Z. Chenmou, *Chem. Phys. Lett.*, 2004, **399**, 461.
11 A. Gurlo, N. Bârsan, M. Ivanovskaya, U. Weimar and W. Göpel, *Sens. Actuators, B*, 1998, **47**, 92.
12 N. Du, H. Zhang, B. D. Chen, X. Y. Ma, Z. H. Liu, J. B. Wu and D. R. Yang, *Adv. Mater.*, 2007, **19**, 1641.
13 J. Liu, T. Luo, F. Meng, K. Qian, Y. Wan and J. Liu, *J. Phys. Chem. C*, 2010, **114**, 4887.
14 E. Li, Z. Cheng, J. Xu, Q. Pan, W. Yu and Y. Chu, *Cryst. Growth Des.*, 2009, **9**, 2146.
15 K. I. Choi, H. R. Kim and J. H. Lee, *Sens. Actuators, B*, 2009, **138**, 497.
16 C. Wang, D. Chen, X. Jiao and C. Chen, *J. Phys. Chem. C*, 2007, **111**, 13398.
17 L. Y. Chen, Y. G. Zhang, W. Z. Wang and Z. D. Zhang, *Eur. J. Inorg. Chem.*, 2008, 1445.
18 H. Zhu, X. Wang, L. Qiang, F. Yang and X. Yang, *J. Phys. Chem. C*, 2008, **112**, 4486.
19 J. Du, M. Yang, S. N. Cha, D. Rhen, M. Kang and D. J. Kang, *Cryst. Growth Des.*, 2008, **8**, 2312.
20 L. Y. Chen and Z. D. Zhang, *J. Phys. Chem. C*, 2008, **112**, 18798.
21 J. Yang, C. Lin, Z. Wang and J. Lin, *Inorg. Chem.*, 2006, **45**, 8973.
22 P. Zhao, T. Huang and K. Huang, *J. Phys. Chem. C*, 2007, **111**, 12890.
23 A. Datta, S.K. Panda, D. Ganguli, P. Mishra and S. Chaudhuri, *Cryst. Growth Des.*, 2007, **7**, 163.
24 Y. Qiu, P. Bellina, L. P. H. Jeurgens, A. Leineweber, U. Welzel, P. Gerstel, L. Jiang, P. A. van Aken, J. Bill and F. Aldinger, *Adv. Funct. Mater.*, 2008, **18**, 2572.
25 N. H. Chou, X. Ke, P. Schiffer and R. E. Schaak, *J. Am. Chem. Soc.*, 2008, **130**, 8140.
26 I. Hussain, S. Graham, Z. Wang, B. Tan, D. C. Sherrington, S. P. Rannard, A. I. Cooper and M. Brust, *J. Am. Chem. Soc.*, 2005, **127**, 16398.
27 T. Yonezawa, S. Onoue and N. Kimizuka, *Langmuir*, 2000, **16**, 5218.
28 K. Esumi, R. Nakamura, A. Suzuki and K. Torigoe, *Langmuir*, 2000, **16**, 7842.
29 D. Li, D. Sutton, A. Burgess, D. Graham and P. D. Calvert, *J. Mater. Chem.*, 2009, **19**, 3719.
30 F. F. Shi, M. Bulkowski and K. C. Hsieh, *Nanotechnology*, 2007, **18**, 265301.
31 P. Singh, S. Kumar, A. Katyal, R. Kalra and R. Chandra, *Mater. Lett.*, 2008, **62**, 4164.
32 E. Hammarberg and C. Feldmann, *Chem. Mater.*, 2009, **21**, 771.
33 N. Patel, R. Fernandes and A. Miotello, *J. Catal.*, 2010, **271**, 315.
34 Y. Qiu, P. Bellina, L. P. H. Jeurgens, A. Leineweber, U. Welzel, P. Gerstel, L. Jiang, P. A. van Aken, J. Bill and F. Aldinger, *Adv. Funct. Mater.*, 2008, **18**, 2572–2583.

35 R. Si, Y. W. Zhang, L. P. You and C. H. Yan, *J. Phys. Chem. B*, 2006, **110**, 5994–6000.
36 W. Yin, J. Su, M. Cao, C. Ni, C. Hu and B. Wei, *J. Phys. Chem. C*, 2010, **114**, 65.
37 X. Liu, L. Zhou, R. Yi, N. Zhang, R. Shi, G. Gao and G. Qiu, *J. Phys. Chem. C*, 2008, **112**, 18426.
38 Z. Zhuang, Q. Peng, J. Liu, X. Wang and Y. Li, *Inorg. Chem.*, 2007, **46**, 5179.
39 Q. Liu, W. Lu, A. Ma, J. Tang, J. Lin and J. Fang, *J. Am. Chem. Soc.*, 2005, **127**, 5276.
40 H. Y. Lai, C. H. Chen and C. F. Lee, *Plasmonics*, 2010, **5**, 233.
41 M. I. Mishchenko, L. D. Travis and D. W. Mackowski, *J. Quant. Spectrosc. Radiat. Transfer*, 1996, **55**, 535.
42 D. W. Mackowski, *J. Opt. Soc. Am. A*, 1994, **11**, 2851.
43 D. W. Mackowski and M. I. Mishchenko, *J. Opt. Soc. Am. A*, 1996, **13**, 2266.
44 D. W. Mackowski and M. I. Mishchenko, *J. Quant. Spectrosc. Radiat. Transfer*, 2011, **112**, 2182.
45 J. Jiang, F. Gu, X. Ren, Y. Wang, W. Shao, C. Li and G. Huang, *Ind. Eng. Chem. Res.*, 2011, **50**, 9003.
46 K. S. Kim, H. Song, S. H. Nam, S. M. Kim, H. Jeong, W. B. Kim and G. Y. Jung, *Adv. Mater.*, 2012, **24**, 792.
47 W. Gopel and K. D. Schierbaum, *Sens. Actuators, B*, 1995, **26**(1–3), 1.
48 F. Lu, Y. Liu, M. Dong and X. P. Wang, *Sens. Actuators, B*, 2000, **66**, 225.
49 S. G. Ansari, P. Boroojerdian, S. R. Sainkar, R. N. Karekar, R. C. Aiyer and S. K. Kulkarni, *Thin Solid Films*, 1997, **295**, 271.
50 G. Korotcenkov, *Mater. Sci. Eng., R*, 2008, **61**, 1.
51 N. Barsan and U. Weimar, *J. Electroceram.*, 2001, **7**, 143.
52 H. Liu, S. P. Gong, Y. X. Hu, J. Q. Liu and D. X. Zhou, *Sens. Actuators, B*, 2009, **140**, 190.